Publications of the Astronomical Society of the Pacific, 131:114505 (8pp), 2019 November https://doi.org/10.1088/1538-3873/ab35c0

A New Approach to Free-form Cluster Lens Modeling Inspired by the JPEG Image Compression Method

Daniel Lam
Leiden Observatory, Leiden University, NL-2300 RA Leiden, The Netherlands; daniellam@strw.leidenuniv.nl
Received 2019 May 31; accepted 2019 July 25; published 2019 October 4

Abstract

This paper proposes a new approach to free-form cluster lens modeling that is inspired by the JPEG image compression method. This approach is motivated specifically by the need for accurate modeling of high-magnification regions in galaxy clusters. Existing modeling methods may struggle in these regions due to their limited flexibility in the parameterization of the lens, even for a wide variety of free-form methods. This limitation especially hinders the characterization of faint galaxies at high redshifts, which have important implications for the formation of the first galaxies and even for the nature of dark matter. JPEG images are extremely accurate representations of their original, uncompressed counterparts but use only a fraction of number of parameters to represent that information. Its relevance is immediately obvious to cluster lens modeling. Using this technique, it is possible to construct flexible models that are capable of accurately reproducing the true mass distribution using only a small number of free parameters. Transferring this well-proven technology to cluster lens modeling, I demonstrate that this "JPEG parameterization" is indeed flexible enough to accurately approximate an *N*-body simulated cluster.

Key words: galaxies: clusters: general – gravitational lensing: strong – methods: numerical

Online material: color figures

1. Introduction

One of the most active research topics on high-redshift galaxies is to measure the faint-end of their luminosity function (LF). The potential downturn (commonly referred to as the "turnover") in the number density of faint galaxies at high redshifts has important implications to many of the following questions: (1) what are the sources that reionized the universe? (2) how do baryonic processes affect star formation efficiency in low-mass halos? and (3) what are the properties of dark matter?

Cluster lenses provide the most promising prospect of detecting the turnover in the faint-end LF because of their high magnification of background sources over modest areas ($\geqslant$1 arcmin^2). This advantage drastically reduces the investment in observational time required, compared with conventional blank, deep fields (Postman et al. 2012; Lotz et al. 2017; Coe et al. 2019). Currently, the potential turnover in the LF is likely still a few magnitudes out of reach of even the state-of-the-art analyses of the deepest cluster-lensed deep field data (Atek et al. 2015a, 2015b, 2018; Laporte et al. 2016; Bouwens et al. 2017; Livermore et al. 2017; Ishigaki et al. 2018; Kawamata et al. 2018). The main challenge to measuring many valuable intrinsic properties of the lensed sources is to construct accurate lens models for magnification correction.

From the perspective of a *user* of lens models, because the underlying truth is unknown, concurrence among lens models is generally taken as an indication of their reliability. Conversely, where lens models show significant differences is also where users start losing confidence in the models. From the point of view of a *modeler*, the accuracy with which various lens modeling methods recover the mass distribution of a cluster can be evaluated through end-to-end tests and modeling challenges. In an impressive effort, Meneghetti et al. (2017) performed exactly such an end-to-end test using two mock clusters, one constructed by superimposing parametric functions together (Ares), and another by an *N*-body simulation (Hera). They constructed a realistic set of data "observing" each mock cluster, employed various modeling techniques to determine their mass distributions, and then compared the recovered mass distributions with the actual distributions. Meneghetti et al. (2017) find that the best performing method (GLAFIC, Oguri 2010) is able to reconstruct the magnification of Hera to within 10% in the median at a true magnification of $\mu_{\rm true} \approx 3$, and within 30% in the median at $\mu_{\rm true} \approx 10$ using strong lensing constraints.

However, one should note that this test is the first of its kind, and so is justifiably simplistic compared with the real universe. For example, Hera is constructed from a dark matter-only *N*-body simulation. In reality, a non-negligible fraction of the cluster mass resides in the hot intracluster gas, and it is not obvious that its spatial distribution should be well-described by any of the commonly chosen parametric functions (e.g., Navarro–Frenk–White (NFW) profile Navarro et al. 1996), especially for merging cluster–cluster collisions, where the gas and dark matter are displaced spatially (Clowe et al. 2006).

Fundamentally, magnification μ depends on the gradients of the scaled deflection field $\boldsymbol{\alpha}$,

$$\mu(\boldsymbol{\theta}) = \left[\det\left(\delta_{ij} - \frac{\partial \alpha_i(\boldsymbol{\theta})}{\partial \theta_j}\right)\right]^{-1}, \tag{1}$$

where δ_{ij} is the Kronecker delta, and $\boldsymbol{\theta}$ is the angular position on the sky. The scaled deflection field in turn depends on the surface mass density Σ,

$$\boldsymbol{\alpha}(\boldsymbol{\xi}) = \frac{D_{ds}}{D_s}\frac{4G}{c^2}\int \Sigma(\boldsymbol{\xi}')\frac{\boldsymbol{\xi} - \boldsymbol{\xi}'}{|\boldsymbol{\xi} - \boldsymbol{\xi}'|^2} d^2\xi', \tag{2}$$

where $\boldsymbol{\xi}$ is the physical position on the lens plane, D_{ds} is the angular diameter distance between the deflector (the cluster lens) and the source, and D_s is the angular diameter distance between the observer ($z = 0$) and the source. The (in)flexibility in the mass model is translated into that of the deflection field, which ultimately limits the accuracy of the modeled magnification.

For parametric models, their flexibility is inherently limited because the parametric halos typically have few free parameters and thus have restricted shapes. For most free-form, or nonparametric models, however, flexibility is still somewhat limited by the particular choice of basis functions that one places on a grid (Diego et al. 2005; Liesenborgs et al. 2006). This is because the mass model is a summation of the basis functions that are required to be nonnegative. As a result, mass models can only be steeper if and only if there is an increase of the total mass of a model. The only truly nonparametric model involves grids of independent pixels, each having its own free parameter (see e.g., Saha & Williams 2004; Coles et al. 2018). Such a model indeed has unlimited flexibility, but the number of free parameters will be unfeasibly large for any practical spatial resolution required to study galaxy clusters. These limitations found in the current landscape of cluster lens modeling call for a new approach.

This paper proposes a new free-form parameterization that can model mass distributions of galaxy clusters with high degrees of accuracy, efficiency, and flexibility. This approach is inspired by the widely used JPEG image compression algorithm, which uses a linear combination of two-dimensional cosine functions to model the original image. The fact that JPEG image compression is able to accurately and efficiently approximate all kinds of images makes it an interesting case to consider for modeling the mass distributions within galaxy clusters.

Compared with existing free-form modeling methods that use *local* basis functions (e.g., Gaussian functions by WSLAP + Diego et al. 2005, 2007; Sendra et al. 2014, and Plummer functions by GRALE Liesenborgs et al. 2006), the *global* JPEG basis functions have the advantage of capturing both small- and large-scale features while using fewer free parameters. For conventional free-form models to better capture small-scale features, it is necessary to shrink the size of the basis functions. At the same time, adjacent basis functions must have sufficient overlap. Otherwise, the lens model will have "clumpy" artifacts. To prevent this problem, the number of basis functions, hence the number of free parameters, must increase. As I will show in this paper, the JPEG parameterization circumvents this cost by using sinusoidal fluctuations of different frequencies that span the entire field of view.

This paper is structured as follows. In Section 2, I explain the core idea of JPEG image compression that is relevant to lens modeling. Next, I describe the lens parameterization, and apply it to model an N-body simulated cluster first using all the pixels of the deflection field as constraint, and then using only 200 random pixels. Section 3 presents the best-fit deflection field models and the reconstructed mass and magnification models. In Section 4 I discuss the strengths and improvement in efficiency of the JPEG parameterization compared with existing free-form lens modeling methods. In Section 5, I provide a summary of the methodology and results.

2. Methodology

2.1. Utility of JPEG Image Compression for Cluster Lens Modeling

I begin by describing the utility of JPEG image for encapsulating information in an efficient way. Without dwelling on every detail of how it works, this section provides a brief description that is relevant to cluster lens modeling.

Depending on the compression ratio, JPEG images can be extremely accurate approximations of their original, uncompressed counterparts. They are often visually indistinguishable from the original images while taking up only 10–20 times less storage space.

The original, uncompressed image is first divided into 8 × 8 pixel blocks. Each of them is approximated separately using the same treatment. A color image consists of a luminosity and a color component. Here, only the approximation for the former is used as an example. Panel (*b*) of Figure 1 shows an 8 pixel × 8 pixel image of a hand-drawn figure smoothed with a Gaussian filter.

At the heart of JPEG compression is a set of $8 \times 8 = 64$ cosine basis functions,

$$g_{i,j}(x, y) = \cos\left(\frac{ix}{2}\right) \times \cos\left(\frac{jy}{2}\right), \tag{3}$$

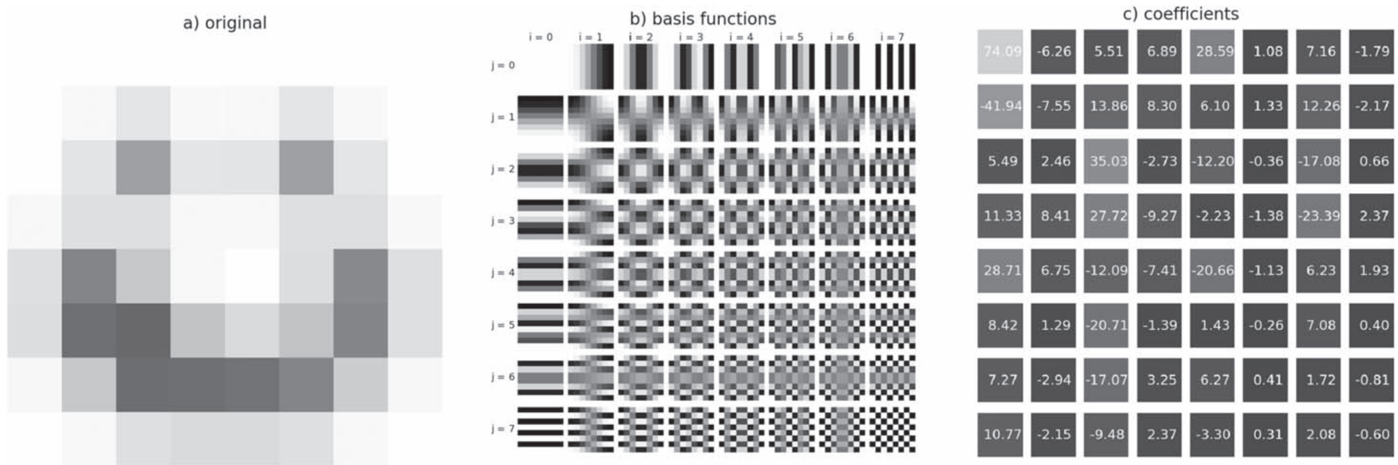

Figure 1. Brief illustration of the JPEG image compression method. a): The original Gaussian-smoothed hand-drawn image. It has a size of 8 pixels by 8 pixels. b): The 64 basis functions used in JPEG image compression. Each basis function is the product of a two-dimensional cosine function varying in the x-direction and one in the y-direction. Products of short-wavelength functions are useful at capturing small-scale features in the image, and vice versa. Each basis function is 8 pixels by 8 pixels across. c): The optimal coefficients of the basis functions such that the original image is best reproduced. The background shading of each sub-panel denotes the absolute amplitude of that coefficient. In this case, the replication is perfect after rounding off the decimals because the cosine basis functions are orthogonal, and so the transformation is invertible. In real-world applications, short-wavelength components can often be discarded to save storage space without significantly degrading the image quality.

where i and j are integers ranging from 0 to 7, while x and y are pixel coordinates and each take eight equally separated values from 0 to 2π. 14 of the basis functions ($j = 0$ and $i > 0$, and $i = 0$ and $j > 0$) consist of two-dimensional cosine functions of various wavelengths that propagate in the x- and y-directions, respectively. Forty-nine of them ($i > 0$ and $j > 0$) are the products of each of these cosine basis functions oscillating in the x-direction with each of those oscillating in the y-direction. The remaining one ($i = j = 0$) is constant over all pixels and simply act as a "floor." Panel (b) of Figure 1 shows what the basis functions look like.

As with most image files, the input image has pixel values ranging from 0 to 255. However, the basis functions range from -1 to $+1$. Therefore, to approximate the image with those basis functions, it has to be centered around 0 by subtracting 128 throughout. In the end, all pixel values are raised by 128 to give the final output.

Each basis function has its own coefficient, which can be negative or positive. They are calculated such that the linear combination of all the basis functions gives the best approximation. This technique central to JPEG image compression is called "discrete cosine transform."

In our example, we found that the original image is best reproduced with the particular set of coefficients listed in panel (c) of Figure 1. In fact, the original image (panel a) of Figure 1) is perfectly reproduced after rounding the pixel values to integers. This is expected because the cosine functions are orthogonal, and so the transformation is invertible. In real-world applications, short-wavelength components can often be discarded without degrading the approximate image much, thus reducing the storage space needed. As one can see, the short-wavelength coefficients are typically smaller in Figure 1(c)). In addition, the human eye is even less sensitive to color changes than to brightness changes. Therefore, compression in color space can be even more aggressive than in luminosity without making much noticeable difference.

This subsection briefly demonstrated how JPEG compression works. For the presented case, the number of free parameters (coefficients), even at high compression, is of the order of the number of pixels. By contrast, in the setting of cluster lens modeling, which I will introduce in the next subsection, a usable lens model should be at least a few hundred pixels across, which means the number of pixels is of the order of a hundred thousand.

Fortunately, as abrupt pixel-to-pixel variations in general are not common in cluster lenses, the number of free parameters can be set drastically lower than the number of pixels, at the expense of ensuring that the information on the smallest spatial scale is correct. Ideally, the number of free parameters should not greatly exceed the number of constraints available, which is about a few hundred for a well-studied Frontier Field-like cluster including weak lensing constraints. This is because models that have many more free parameters than constraints tend to show large erroneous fluctuations in unconstrained regions.

2.2. Example Simulated Cluster

To illustrate how a JPEG parameterization would work with a cluster mass distribution, I use as an example the lensing cluster *Hera*, which is identified in a collisionless *N*-body cosmological simulation (Planelles et al. 2014). It is used in Meneghetti et al. (2017) to compare how well various lens modeling methods work. The cluster is located at a redshift of $z = 0.507$ and has a total mass of $M = 9.4 \times 10^{14} h^{-1}\ M_{\odot}$. Its virial region is well resolved with ≈10 million dark matter particles. For this study, the central $2\overset{'}{.}22 \times 2\overset{'}{.}22$ region of its surface mass density is rebinned to 500×500 pixels. Panel (*K*) in Figure 2 shows its dimensionless surface mass density (convergence κ) at $z = 9$. The scaled deflection field (panels (*A*) and (*F*)) is then computed pixel-by-pixel.

2.3. Parameterization of Cluster Mass Distribution

In this study, I will experiment with modeling the surface mass density of clusters using $20 \times 20 = 400$ cosine basis functions, which have the same form as in Equation (3), except i and j now range from 0 to 19. Their coefficients can be positive or negative—allowing for greater flexibility than existing free-form lens parameterizations. Individual weighted basis functions may have negative mass at certain regions, but the first basis function, which has $i = j = 0$, can act as a floor, and "raise" the final mass model out of negative mass values provided there are sufficient constraints.

2.3.1. Fitting the Entire Deflection Field: Model-1

The full set of coefficients that best represents the surface mass density is determined in an iterative process (referred to as optimization thereafter). I derive it by fitting to the deflection field because in practice, that, along with the source positions, are what is being directly constrained by the strong lensing observations (other observational constraints such as weak lensing shear and relative magnification among multiple images are related to *derivatives* of the deflection field). The total absolute difference between the true and the model deflection field is minimized using the `SLSQP` algorithm in `scipy.minimize` with all initial coefficients equal zero. The resultant best-fit model is denoted as Model-1.

To speed up the optimization of the lens model, instead of integrating the deflection field from the mass model at each step, the deflection field of each of these basis functions are computed in advance, and are simply weighted by their coefficients and then summed to produce the overall deflection field model at each step. Note that, unlike the models constructed in Meneghetti et al. (2017), this model is not derived by trying to match mock observables based on a cluster mass distribution. Instead, the mass distribution is determined by directly fitting the deflection field. Therefore, the results for Model-1 only demonstrate the best achievable outcome using a JPEG-like representation.

2.3.2. Fitting the Sampled Deflection Field: Model-2

While Model-1 is optimized over all 250,000 pixels, in practice, lensing constraints are available over a much smaller number of points within the overall high-magnification area. As such, it is useful to consider a representation which is more consistent with what one would derive from actual lensing constraints. For this reason, I optimize the deflection field model for Hera at only 200 sample points, which roughly equals the number of multiple images in a well-observed cluster. This best-fit model is denoted as Model-2. Like Model-1, Model-2 also consists of 400 basis functions. The 200 points of constraint are randomly and uniformly distributed within a central circular region of $7\overset{'}{.}2$ radius. The placement of these sampling points covers most of the critical curves at $z = 9$, and acts as a heuristic approximation to the spatial distribution of multiple images (including radial images) of sources over a range of redshifts. Actual multiple images are not distributed uniformly. They tend to straddle the critical curves and concentrate around the more massive galaxies. For applications to real data, it is expected the lens models would be better constrained in regions where there are a higher number density of multiple images.

3. Results

3.1. Accuracy and Precision of Model-1

Panels (*B*) and (*G*) in Figure 2 show the horizontal and vertical components of the best-fit deflection field model at $z = 9$, respectively. All the features of the deflection field are accurately reproduced with the exception of those near high-density, compact halos. The differences between the true and model deflection field can be seen more clearly in panels (*D*) and (*I*), where the contrast is increased by 50 times and color-coded. In regions where multiple images are present, the difference is in general within $1''$. The difference is largest ($\approx 6''$) near the central regions of the most massive halos. These discrepancies arise because small-scale features such as the cores of galaxy halos cannot be accurately reproduced by even the basis functions with the shortest "wavelengths." In this case, one half of the shortest wavelength equals $7''$, which is the smallest "feature size" that can be modeled by 20×20 basis functions. Any structures smaller than this length scale cannot be modeled. The number of free parameters are chosen such that it is slightly higher than the typical number of constraints available in a well-studied lensing cluster. As a result, the magnitude of the deflection is underestimated near the high-density, compact regions.

The same problem is evident from panel (*N*) of Figure 2, which shows the percentage difference between the true and best-fit convergence at $z = 9$. The true convergence is in general reproduced to within a few percent, but can be underestimated by $>10\%$ at the cores of galaxy halos. Some local over-estimation around an isolated halo toward the

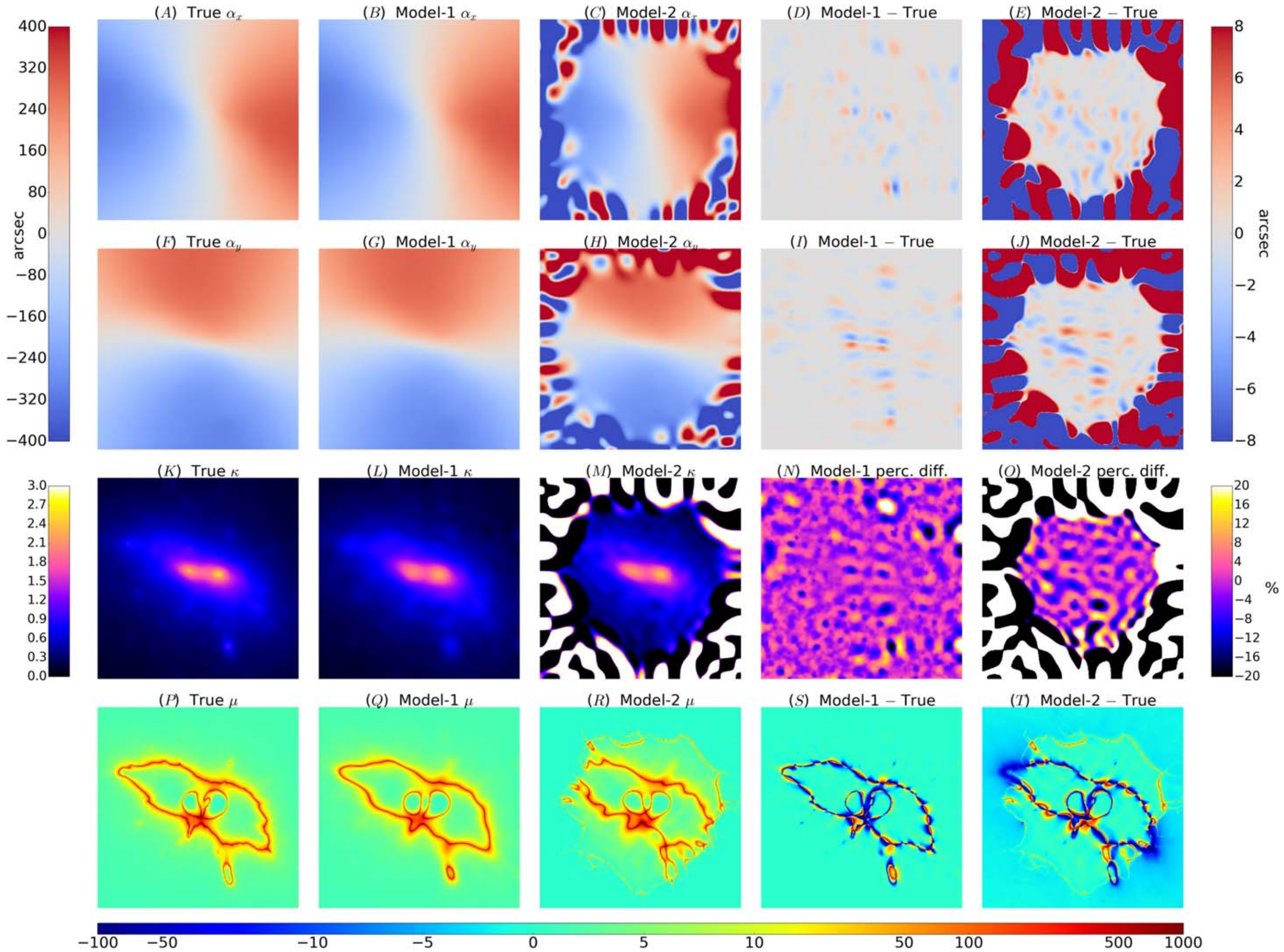

Figure 2. Comparing the true deflection field (first row: α_x, second row: α_y), convergence κ (third row), and magnification μ (fourth row) of an *N*-body simulated cluster, *Hera*, with those of Model-1 and Model-2 representations. The first column shows the true quantities; the second shows the best-fit model constructed by minimizing the total difference between the true and model deflection field; the third shows the best-fit model constructed by minimizing the difference in deflection at only 200 randomly sampled locations; the fourth and fifth columns highlight the differences between the models and the truth. Values in panels *A* to *C*, *F* to *H*, and *K* to *M* are denoted by the color scales on the left while those in the difference panels are denoted by the color scales on the right. Values of all panels in the fourth row are denoted by the same color bar at the bottom. The first best-fit model is constructed by minimizing the total difference in deflection (second column). It demonstrates that the parameterization with cosine basis functions is indeed flexible enough to accurately capture most details of the lens. In terms of deflection, the discrepancy (panels (*D*) and (*I*)) is typically less than $1''$ with the exception for regions immediately next to the core regions of galaxy halos, where the discrepancy can reach $6''$. This is because the cosine basis functions are unable to capture any details smaller than half the shortest wavelength, which is $7''$ in this case. This same problem is evident in panel (*N*), which shows the percentage difference between the true (panel *K*) and the model convergence (panel *L*), where all the core regions of galaxy halos are underestimated by $>$10%. The global mass model, however, is accurate to within a few percent. The true magnification (panel *P*) is also mostly accurately captured by the model (panel *Q*), with the exception of small-scale fluctuations. There is neither significant systematic discrepancies in the location of the critical curves nor over large-scale, low-magnification regions. The second best-fit model is constructed by minimizing the difference in deflection at only 200 locations. The positions are randomly and uniformly distributed within a central circular region to imitate a sampled constraint of the deflection field with multiply lensed galaxies. The discrepancies between this sampled model and the truth is slightly larger in the constraint region but still retains most of the features. Beyond the constrained region, the best-fit model shows large fluctuations, as smoothness is not a criterion implemented in the optimization process. The color bar for magnification at the bottom is roughly linear between -10 and $+10$, and is logarithmic beyond this range. All quantities are calculated at a source redshift of $z = 9$. Each panel spans a field of view of $2\overset{\prime}{.}22 \times 2\overset{\prime}{.}22$.

(A color version of this figure is available in the online journal.)

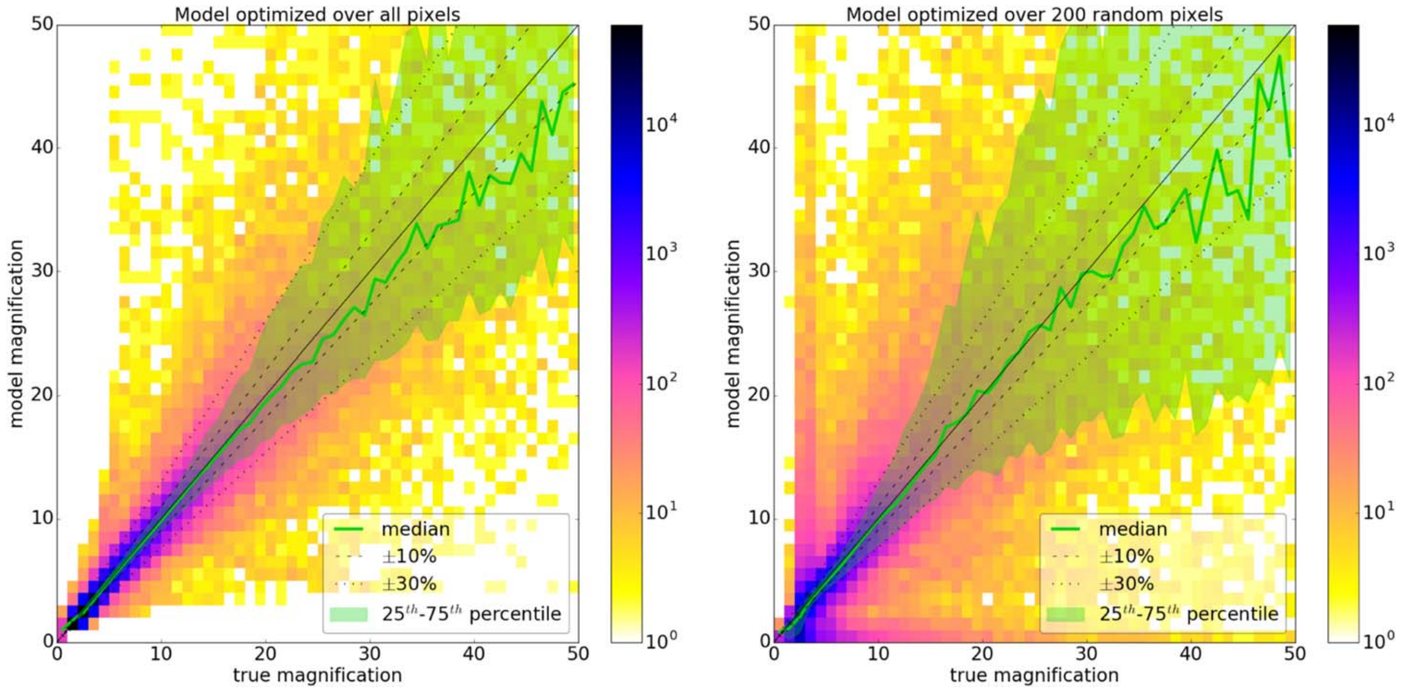

Figure 3. Model vs. true magnification. The colored surface density plot shows the distribution of pixels. *Left*: the best-fit model constructed by minimizing the total difference between the true and model deflection field (Model-1). *Right*: the best-fit model constructed by minimizing the difference in deflection at 200 random locations (Model-2). Only the constrained region is shown for Model-2. The green line shows the median model magnification as a function of true magnification. The green shaded region shows the distribution within the 25th and 75th percentiles. The solid black line is the one-to-one line. The dashed and the dotted black lines denote ±10% and ±30% deviation from the true magnification, respectively. The median magnification of Model-1 shows a slight underestimation beyond a true magnification of 20 but mostly remains within 10% accurate all the way out to 40. The precision (green shaded area) is within 10% below a true magnification of 10, and within 30% below 30. With much fewer constraints, the median of Model-2 is similarly accurate to 10% in the median up to 40 times magnification. However, the precision degrades much more quickly—the 25th–75th percentile exceeds 10% of the true magnification beyond a magnification of 5, and 30% beyond a magnification of 12. This plot is made following Figures 23 and 24 in Meneghetti et al. (2017) for convenient comparison.

(A color version of this figure is available in the online journal.)

bottom of the field of view is caused by the inability to reproduce highly elliptical galaxy halos given the current number of basis functions (a larger number of basis functions will better reproduce small-scale features, including ellipticity).

The magnification map is accurately reproduced except the smallest features, as shown in panels (*P*), (*Q*), and (*S*) of Figure 2. There is neither significant systematic offsets in the location of the critical curves nor in large-scale, low-magnification regions. Figure 3 plots, pixel-by-pixel, the model magnification versus the true magnification. The median model magnification is in general accurate to within 10% to $\mu_{\rm true} = 40$ with only slight systematic deviation of a few percent beyond $\mu_{\rm true} > 20$. Following the convention of Meneghetti et al. (2017), precision is defined as the 25th and 75th percentiles of the distribution of μ–$\mu_{\rm true}$, which is within 10% up to $\mu_{\rm true} = 10\%$ and 30% up to $\mu_{\rm true} = 30$.

3.2. Accuracy and Precision of Model-2

Figure 2 also compares the true deflection field, convergence, and magnification with those of Model-2. It shows larger differences from the truth than the one optimized using all pixels, but still recovers most of the prominent features within the constrained region. We also remark that there are no regions with formally negative mass densities inside the constrained region, even though we do not explicitly force this to be the case. Beyond where constraints exist, the best-fit model shows large fluctuations as smoothness is not a criterion in the optimization process.

The right panel of Figure 3 shows the comparison between the model and the true magnification for pixels within the constrained region. Model-2 shows a larger dispersion compared with Model-1. The median model magnification is still accurate to within 10% up to 40× magnification. However, the precision of Model-2 degrades much more quickly—the 25th–75th percentile exceeds 10% and 30% difference at magnification of 5× and 12×, respectively.

4. Discussion

What has been demonstrated in this paper is simply a direct fit of a simulated surface mass density with the cosine basis functions. By no means is it a working lens modeling code. Nevertheless, it shows the capability of this "JPEG" approach, which so far appears to be a promising choice of parameterization for free-form lens modeling. The biggest hurdle needed to be overcome to make this proof of concept into a functioning lens modeling code is to optimize the lens model with lensing constraints. This will be described in a future paper (D. Lam et al. 2019, in preparation).

4.1. Comparison with other Free-form Hera Models

A significant point of this study is to present an approach that efficiently encapsulates information about the surface mass density of a galaxy cluster. Therefore, it is useful to compare our approach to others used in the literature. The present JPEG representation of the Hera cluster makes use of 400 free parameters.

Here I compare it with the six free-form models from Meneghetti et al. (2017). In that study, a number of lens modeling methods are benchmarked by reconstructing lens models for *Hera* using simulated lensing constraints. 19 background galaxies are strongly lensed into 65 multiple images, and additional background galaxies are weakly lensed with a surface number density of $\approx$14 arcmin^{-2}.

The Bradac–Hoag model, constructed using the method SWUnited (Bradač et al. 2005, 2009), has 5497 free parameters. These free parameters correspond to values in the gravitational potential over the same number of points. These points are distributed over an iterative, multi-resolution grid which is coarse in the cluster outskirts where constraints are sparse, and fine in the cluster center, where the brightest cluster galaxies and most multiple images reside. In addition to the 65 multiple images, this model is also constrained by 2102 weak lensing ellipticity measurements.

Two out of three variants of Diego models, and the Lam model, constructed using the method WSLAP+ (Diego et al. 2005, 2007; Sendra et al. 2014), have 1027 free parameters. WSLAP+ models the mass distribution primarily as the summation of a grid of two-dimensional Gaussian functions. The two Diego models and the Lam model aforementioned are evaluated on regular grids. The third variant of the Diego models is evaluated on an adaptive grid and has only 304 free parameters. The grid of the adaptive Diego model has varying resolution over the field of view. The resolution of the grid is iteratively increased over regions where the previous optimization step found more mass compared with other regions. The adaptive grid allows the model to perform comparably with regular-grid models using roughly only half the number of free parameters. A second component of WSLAP+ accounts for small-scale mass features, that is, cluster galaxies. All three Diego models use the light profile of the cluster galaxies as the second component while the Lam model uses an NFW parameterization.

The number of free parameters in the set of GRALE (Liesenborgs et al. 2006) models ranges from 600 to a couple of thousands[1] The mass model comprise of a uniform mass sheet and a large number of projected Plummer spheres. In addition to using multiple images as constraints, the GRALE model is also constrained by "null space," which are regions where no strongly lensed galaxies are present.

In summary, the JPEG parameterization appears to be able to capture features at both small- and large-scales while using significantly fewer free parameters compared with most existing free-form lens modeling methods. Although the number of free parameters can be chosen arbitrarily, and that the JPEG models presented here are constructed in an entirely different way from the ones in Meneghetti et al. (2017), a brief comparison nonetheless gives the reader a better idea of the potential gain in efficiency that the JPEG approach has.

4.2. Progressive Optimization

Although not currently implemented, parameterizing the lens model as a linear combination of cosine basis functions allows convenient *progressive* optimization of the lens model. While each of the two models takes 1.5 days to optimize on an ordinary desktop computer with a 6-core, 3.5 GHz CPU and 8 GB of RAM, optimizing with lensing constraints will likely take much longer. The reason is that the chi-squared "landscape" in the parameter space is likely to be much more complex with lensing constraints, thus the optimization algorithm will take longer to find the next direction of descent.

Progressive optimization mitigates this problem. To begin, the lens model is only parameterized with a handful of long-wavelength basis functions. Optimizing a small number of free parameters will quickly yield a lens model that is roughly correct on the large scale. These optimized coefficients can then be used as the initial solution for the next optimization, which adds a few shorter-wavelength basis functions to the model. Using this strategy, the optimization algorithm will start exploring the parameter space closer to the global minimum compared with the case where it starts at some other arbitrary or random locations, thus shortening the time required to reach convergence.

5. Summary

In this paper, I propose a new approach to free-form cluster lens modeling inspired by the parameterization used in JPEG image compression. Unlike the conventional approach to free-form cluster lens modeling, which places two-dimensional basis functions on a grid, this approach uses orthogonal cosine

[1] The initial number of free parameters range from 600 to 1000, which increases during optimization. The exact final number of free parameters is not stated in Meneghetti et al. (2017).

functions of different wavelengths and their products as basis functions.

This approach has the advantage of being able to capture a wider range of mass gradients and feature sizes (from $2'$ to $7''$) in the lens model while using a moderate number of free parameters. As explained in Section 1, flexibility is key to obtaining accurate magnification, which many other science goals rely on, such as the exciting prospect of detecting faint-end turnovers in the high-redshift galaxy LFs.

As a proof of concept, I demonstrate the capability of this approach by directly fitting the deflection fields of 400 cosine basis functions to that of an *N*-body simulated cluster, *Hera* (Meneghetti et al. 2017). For a well-studied, Frontier Field-like cluster, this amount of free parameters roughly matches that of available constraints (including weak lensing constraints). The overall morphology of the mock lens is accurately reproduced except for the central regions of individual halos. This is because the cosine basis functions are unable to capture any details smaller than half of their shortest wavelength.

The accuracy of the best-fit model is quantified by the median model magnification, which varies within 10% of the true magnification out to a magnification of 40. The precision is quantified by the 25th–75th percentile, which is within 10% up to $\mu_{\rm true} = 10\%$ and 30% up to $\mu_{\rm true} = 30$.

A second, more realistic model is obtained by fitting the basis functions to a sample of only 200 positions drawn randomly from the strong lensing region and of use for demonstrating use of the "JPEG approach" in a more realistic setting. It has a similar accuracy within the constrained region although precision degrades more quickly—the 25th–75th percentile exceeds 10% and 30% at 5 and 12 times magnification, respectively. These encouraging capabilities show that this "JPEG lensing" approach could be a promising technique in future cluster lens modeling.

In the future, I plan to reconstruct the simulated *N*-body cluster, *Hera*, with the JPEG parameterization using multiple images and weak lensing ellipticity measurements as constraints. Once that is demonstrated, a more streamlined progressive optimization will be implemented, which will potentially result in faster optimization and more accurate models.

The author thanks Rychard Bouwens and Jose Diego for valuable feedback on both the write-up and science of the manuscript, Jori Liesenborgs, Liliya Wiliams, Dan Coe, and Masamune Oguri for stimulating discussions, Massimo Meneghetti for coordinating the HFF comparison project, and the HFF community for contributing to the conversation with all their collective efforts.

ORCID iDs

Daniel Lam https://orcid.org/0000-0002-6536-5575

References

Atek, H., Richard, J., Jauzac, M., et al. 2015a, ApJ, 814, 69
Atek, H., Richard, J., Kneib, J.-P., et al. 2015b, ApJ, 800, 18
Atek, H., Richard, J., Kneib, J.-P., et al. 2018, MNRAS, 479, 5184
Bouwens, R., Oesch, P., Illingworth, G., et al. 2017, ApJ, 843, 129
Bradač, M., Schneider, P., Lombardi, M., & Erben, T. 2005, A&A, 437, 39
Bradač, M., Treu, T., Applegate, D., et al. 2009, ApJ, 706, 1201
Clowe, D., Bradač, M., Gonzalez, A., et al. 2006, ApJ, 648, 109
Coe, D., Salmon, B., Bradač, M., et al. 2019, arXiv:1903.02002
Coles, J. P., Read, J. I., & Saha, P. 2018, GLASS: Parallel, free-form gravitational lens modeling tool and framework, Astrophysics Source Code Library, ascl:1806.009
Diego, J. M., Protopapas, P., Sandvik, H. B., & Tegmark, M. 2005, MNRAS, 360, 477
Diego, J. M., Tegmark, M., Protopapas, P., & Sandvik, H. 2007, MNRAS, 375, 958
Ishigaki, M., Kawamata, R., Ouchi, M., et al. 2018, ApJ, 854, 73
Kawamata, R., Ishigaki, M., Shimasaku, K., et al. 2018, ApJ, 855, 4
Laporte, N., Infante, L., Troncoso Iribarren, P., et al. 2016, ApJ, 820, 98
Liesenborgs, J., De Rijcke, S., & Dejonghe, H. 2006, MNRAS, 367, 1209
Livermore, R., Finkelstein, S., & Lotz, J. 2017, ApJ, 835, 113
Lotz, J. M., Koekemoer, A., Coe, D., et al. 2017, ApJ, 837, 97
Meneghetti, M., Natarajan, P., Coe, D., et al. 2017, MNRAS, 472, 3177
Narayan, R., & Bartelmann, M. 1996, arXiv:astro-ph/9606001
Navarro, J., Frenk, C., & White, S. 1996, ApJ, 462, 563
Oguri, M. 2010, PASJ, 62, 1017
Planelles, S., Borgani, S., Fabjan, D., et al. 2014, MNRAS, 438, 195
Postman, M., Coe, D., Benítez, N., et al. 2012, ApJS, 199, 25
Saha, P., & Williams, L. L. R. 2004, AJ, 127, 2604
Sendra, I., Diego, J. M., Broadhurst, T., et al. 2014, MNRAS, 437, 2642